Physics of Fluids ARTICLE pubs.aip.org/aip/pof

Velocity modulation on the linear instability of liquid jets in ambient gas

Cite as: Phys. Fluids **36**, 012117 (2024); doi: 10.1063/5.0181477
Submitted: 16 October 2023 · Accepted: 14 December 2023 ·
Published Online: 9 January 2024

Ran Qiao (乔然),[1] Chengxi Zhao (赵承熙),[1] Zhaodong Ding (丁兆东),[2] Kai Mu (穆恺),[1,a)] and Ting Si (司廷)[1]

AFFILIATIONS

[1]Department of Modern Mechanics, University of Science and Technology of China, Hefei 230026, People's Republic of China
[2]School of Mathematical Science, Inner Mongolia University, Hohhot, Inner Mongolia 010021, People's Republic of China

[a)]Author to whom correspondence should be addressed: mukai@ustc.edu.cn

ABSTRACT

The linear instability analysis of liquid jets with periodic velocity modulation in the ambient gas is carried out. Utilizing the viscous potential theory and the Floquet theory, an analytical dispersion relation for the perturbation growth can be obtained. Due to the parametric resonance caused by velocity modulation, the oscillatory Kelvin–Helmholtz instability (OKHI) can be triggered in the short-wavelength region, leading to the competition between the OKHI and the intrinsic Rayleigh–Plateau and Kelvin–Helmholtz instability (RP-KHI). The parametric study shows that the increase in the velocity oscillation amplitude can enhance the jet instability and lead to the transition of the instability mechanism from the RP-KHI to the OKHI. The velocity oscillation frequency mainly affects the growth of the OKHI. Specifically, the maximum growth rates of perturbation vary with the oscillation frequency at moderate frequencies due to the competition between the RP-KHI and the OKHI, whereas they converge to constant values as the frequency either increases or decreases continuously. The increase in the Weber number promotes the RP-KHI and the OKHI simultaneously, and the jet breakup is dominated by the axisymmetric perturbation of the RP-KHI consistently. The increase in the Reynolds number enhances the jet instability, but hardly affects unstable wavenumber regions. By comparing the maximum growth rates of axisymmetric and non-axisymmetric perturbations, the predominant mode of the jet instability can be identified. Considering variations in the velocity oscillation amplitude and frequency, the transition between the RP-KHI and the OKHI can be predicted by a phase diagram.

I. INTRODUCTION

The fragmentation and atomization of liquid jets in ambient gas environment commonly exist in a variety of industrial applications, including fuel injection,[1–3] spray coating,[4–6] and pesticide spraying.[7,8] To enhance the efficiency of atomization, liquid jets are usually propelled into the gas environment with high velocity, and the aerodynamic stress induced by the velocity difference between the liquid jet and the gas environment plays a significant role in the jet breakup. Moreover, due to the perturbation of the surrounding acoustic field or the pulsation of jet flow rate, periodic velocity oscillation always exists during the injection of liquid jet through the nozzle. Consequently, investigating the instability characteristics of liquid jets under velocity modulation is of vital significance for practical applications.

The breakup characteristics of the liquid jet are determined by the cooperative effects of liquid inertia, viscosity, surface tension, and aerodynamic forces.[9,10] When the velocity of the liquid jet is relatively low, the jet breakup is dominated by the surface tension.[11–13] Once the jet velocity keeps increasing, the aerodynamic force brought by the gas surroundings tends to dominate the jet instability. A continuous increase in jet velocity can eventually lead to the atomization regime, where the jet surface disintegrates into droplets at the nozzle exit directly. Generally, there are two kinds of instability mechanisms involved in the jet breakup, including the Rayleigh–Plateau instability (RPI), which is induced by the surface tension, and the Kelvin–Helmholtz instability (KHI), which is caused by the shear stress between the liquid jet and the ambient gas. It has been summarized that the jet breakup at the Rayleigh regime is mainly attributed to the RPI, whereas the KHI plays an increasingly important role with the increase in jet velocity and finally dominates the jet breakup under the atomization regime.[10] The RPI leads to the jet breakup with long-wavelength disturbances, and the diameters of produced droplets are comparable with the jet diameter; while the KHI leads to the domination of short-wavelength disturbance during jet breakup, resulting in much smaller produced droplets compared to the jet diameter.

Numerous investigations have been conducted to study the atomization characteristics of high-speed liquid jets. The development of

surface waves on the liquid jet under a high Reynolds number was observed by the experiments of Hoyt and Taylor,[14,15] and the instability characteristics of surface waves were predicted by an inviscid instability analysis. The effect of aerodynamic force on jet instability was investigated by changing the pressure of ambient air, revealing the significant enhancement of the jet instability due to the aerodynamic force.[16] Although the breakup of high-speed liquid jets presents some turbulent characteristics, the laminar jet instability theory was found to be able to give a reasonable prediction.[17] It was found that the existence of surface waves would amplify disturbance with a given frequency,[18] and the growth rates of surface waves vary with the breakup regimes.[19] The fine structures of water jet atomization were observed experimentally.[20] Several numerical studies revealed the abundant dynamics of jet atomization, in which the evolutions of the jet surface were resolved using various interface tracking methods, such as the front tracking method,[21] the volume-of-fluid method,[22,23] and the diffuse interface method.[24] Apart from the investigations of a free liquid jet breakup, the co-flowing air stream was also employed to enhance the shear effect at the jet surface, which contributes to improving the atomization efficiency.[25,26] The extra fields have also been employed to modulate the atomization process, including the electric field,[27,28] the optical field,[29,30] the acoustic field,[31,32] and the thermal field.[33,34]

During the fluid ejection from a nozzle, external perturbations on the liquid jet or the gas surroundings were found to significantly influence atomization efficiency. Generally, the external perturbations can be categorized into two groups, consisting of the transverse and the longitudinal ones. The transverse perturbation can be induced by the acoustic field in the gas environment. It was observed that the liquid jet can evolve to the flattened configuration in transverse acoustic field.[35] The effect of acoustic frequency on the deformation of liquid jets was investigated by experiments, and the theoretical model was also built to describe the jet instability.[36] The atomization of liquid oxygen jets under transverse acoustic perturbation was studied experimentally, in which the physical mechanisms of combustion instabilities were analyzed.[37] Apart from experiments, large eddy simulations were conducted to investigate the dynamics of liquid jets under a transverse acoustic field.[38–40] These studies indicated that the flattened structure of the jet surface commonly exists, and the intact jet length could be reduced by enhancing the intensity of acoustic perturbation. The influence of transverse acoustic perturbation on jet instability has been summarized in detail in the review article by O'Connor *et al.*[41]

Regarding the jet instability under longitudinal perturbations, the oscillation of velocity can be loaded both at the liquid jet or the co-flowing gas surrounding. It has been found that the temporal variation of fluid velocities can result in the oscillatory Kelvin–Helmholtz instability (OKHI).[42,43] Considering the acoustic oscillation on the co-flowing gas, it was found that the parametric instability can be triggered in the short-wavelength region, and the amplitude and frequency of velocity perturbations play significant effects on the jet instability.[44,45] Heister *et al.*[46] carried out numerical simulations using the boundary element method to investigate the effect of the acoustics perturbation on the jet breakup length and droplet sizes for axisymmetric situations. The breakup characteristics of liquid jets under longitudinal inlet velocity modulation were also investigated. In the Rayleigh breakup regime where the jet velocity is relatively low, the jet breakup can be synchronized with the periodic modulation, resulting in the generation of uniformly sized droplets.[47–49] For high-speed liquid jets, several numerical simulations have been performed to analyze the breakup dynamics under velocity modulation.[46,50,51] It was observed that the breakup of liquid threads and the formation of hole structure on the surface can result in plenty of tiny bubbles, which enhance the efficiency of the jet breakup. Yang and Turan[50] investigated effects of the velocity oscillation frequency and the amplitude on jet instability by three-dimensional numerical simulations. They found that there exist three typical response dynamics of jet breakup as the frequency changes, and the liquid jet is more sensitive to the perturbation with low frequency. On the contrary, perturbations with high frequency have little influence on jet atomization, unless the perturbation amplitude is quite large.

To the best of our knowledge, the influences of inlet velocity modulation on the instability characteristics of high-speed liquid jets have mainly been investigated by numerical simulations. The mechanisms of jet breakup under the inlet velocity modulation are far from being interpreted systematically, especially how the modulation parameters (such as the velocity oscillation amplitude and frequency) affect the perturbation growth of liquid jets. Furthermore, the fundamental mechanism of jet instability related to the external velocity modulation needs to be uncovered. Motivated by these limitations, this work carries out a linear instability analysis to study the liquid jet ejecting into a quiescent gas environment under periodic inlet velocity modulation, considering the temporal development of initial perturbations and the transition between different instability mechanisms. This paper is organized as follows. Section II illustrates the physical model and mathematical description of our work. The results and discussion are given in Sec. III, in which the effects of various control parameters are examined, and the transition of the predominate modes is analyzed. Finally, major conclusions are summarized in Sec. IV.

II. PROBLEM FORMULATION

A. Physical model and dimensionless parameters

Figure 1 shows the sketch map of the theoretical model, in which a liquid jet with radius R under periodic velocity oscillation $\bar{U}_1(\bar{t}) = \bar{U}_1 + \Delta\bar{U}\cos(\bar{\omega}_s\bar{t})$ is injected into quiescent gas surroundings, where $\bar{t}$ denotes the time, and $\bar{\omega}_s$ is the angular frequency of oscillation. The dynamical viscosities and densities are defined as μ_i and ρ_i, where $i = 1, 2$ stand for the liquid jet and the ambient gas, respectively. The surface tension between the liquid jet and the gas surroundings is

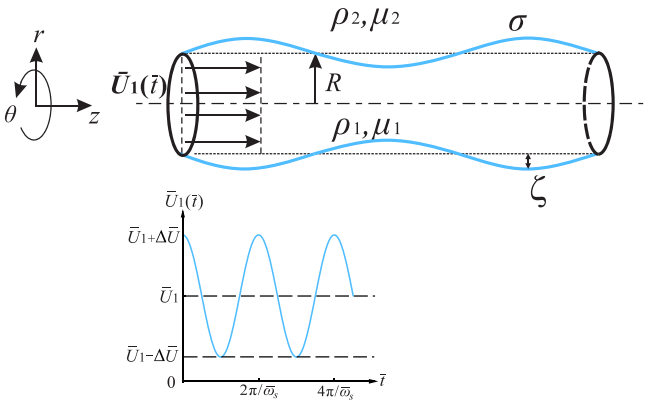

FIG. 1. Sketch of the liquid jet with periodic velocity oscillation of $\bar{U}_1(\bar{t}) = \bar{U}_1 + \Delta\bar{U}\cos(\bar{\omega}_s\bar{t})$.

defined as σ. The physical model is considered in a three-dimensional cylindrical coordinate system (z, r, θ), where z, r, and θ stand for the axial, radial, and azimuthal directions, respectively. The velocity components at the axial, radial, and azimuthal directions are denoted as u, v, and w, and the displacement of the surface is defined as ζ, respectively. The characteristic phase is chosen as the liquid jet, and the characteristic length, velocity, time, and pressure are chosen as R, $\bar{U}_1$, $R/\bar{U}_1$, and $\rho_1\bar{U}_1^2$, respectively. Therefore, the dimensionless parameters involved can be defined as the Reynolds number $Re = \rho_1 R\bar{U}_1/\mu_1$, the Weber number $We = \rho_1 R\bar{U}_1^2/\sigma$, the viscosity ratio $\mu_{21} = \mu_2/\mu_1$, and the density ratio $\rho_{21} = \rho_2/\rho_1$. The dimensionless inlet velocity can be denoted as $U_1(t) = 1 + \Delta U\cos(\omega_s t)$, where ΔU and ω_s are the dimensionless amplitude and angular frequency of the velocity oscillation, and t is the dimensionless time.

B. Linear instability analysis

The linear instability analysis is commonly implemented to investigate the development of initial small perturbations added on the basic flow. The dimensionless governing equations of perturbation for both the liquid jet and the gas surroundings are

$$\nabla\cdot\boldsymbol{u}_i = 0, \quad \frac{\partial \boldsymbol{u}_i}{\partial t} + (\boldsymbol{U}_i\cdot\nabla)\boldsymbol{u}_i = -\left(\frac{1}{\rho_{21}}\right)^{\delta_{2i}}\nabla p_i + \frac{1}{Re}\left(\frac{\mu_{21}}{\rho_{21}}\right)^{\delta_{2i}}\nabla^2\boldsymbol{u}_i, \tag{1}$$

where $\nabla^2 = \frac{\partial^2}{\partial r^2} + \frac{1}{r}\frac{\partial}{\partial r} + \frac{\partial^2}{\partial z^2} + \frac{1}{r^2}\frac{\partial^2}{\partial\theta^2}$, $\boldsymbol{u}_i$ is the perturbation velocity, p_i is the perturbation pressure, and δ is the Kronecker delta function, respectively. As this study considers the high-speed liquid jets, the viscous potential theory[52] is utilized to simplify the governing equations. The viscous potential theory ignores the viscous effect inside the liquid jet and the ambient gas, and only considers the fluid viscosities on the dynamical boundary conditions of the fluid surface, which enables us to derive an explicit analytical dispersion relation of perturbation development. It has been indicated that the results of viscous potential theory converge to the inviscid cases if the Reynolds number is high enough [e.g., $Re \sim O(10^3)$ or even larger] and maintains most of the characteristics of full viscous theory for moderate values of Reynolds number [e.g., $Re \sim O(10^1)$ and $O(10^2)$].[52,53] As the viscous terms in the governing equations are ignored, the perturbation velocity fields of liquid jet and gas surroundings can be represented by the velocity potential functions ϕ_i $(i = 1, 2)$, where $\boldsymbol{u}_i = \nabla\phi_i$. The dimensionless governing equations can be represented as

$$\nabla^2\phi_i = 0, \quad \frac{\partial\phi_i}{\partial t} + (\boldsymbol{U}_i\cdot\nabla)\phi_i = -\left(\frac{1}{\rho_{21}}\right)^{\delta_{2i}}p_i. \tag{2}$$

The corresponding boundary conditions include the consistent condition at the symmetric axis $r = 0$, i.e.,

$$\frac{\partial\phi_1}{\partial r} = \frac{\partial p_1}{\partial r} = 0, \tag{3}$$

and the kinetic and dynamical boundary conditions at the surface $r = 1 + \eta$,

$$\frac{\partial\phi_1}{\partial r} = \frac{\partial\eta}{\partial t} + U_1(t)\frac{\partial\eta}{\partial z}, \tag{4}$$

$$\frac{\partial\phi_2}{\partial r} = \frac{\partial\eta}{\partial t}, \tag{5}$$

$$p_1 - \frac{2}{Re}\frac{\partial^2\phi_1}{\partial r^2} - p_2 + \mu_{21}\frac{2}{Re}\frac{\partial^2\phi_2}{\partial r^2} = \frac{1}{We}\left(-\frac{\partial^2\eta}{\partial z^2} - \eta + n^2\eta\right), \tag{6}$$

and the far-field conditions at $r \to \infty$, i.e.,

$$\frac{\partial\phi_2}{\partial r} = 0, \quad p_2 = 0, \tag{7}$$

where η stands for the dimensionless displacement of the surface.

The potential flow functions can be assumed to have the following form, i.e.,

$$\phi_1 = \Phi_1(r)A(t)\exp(\mathrm{i}kz + \mathrm{i}n\theta), \quad \phi_2 = \Phi_2(r)B(t)\exp(\mathrm{i}kz + \mathrm{i}n\theta). \tag{8}$$

Considering the continuity equations and the boundary conditions of Eqs. (3) and (7), the potential flow functions can be written as

$$\phi_1 = I_n(kr)A(t)\exp(\mathrm{i}kz + \mathrm{i}n\theta), \quad \phi_2 = K_n(kr)B(t)\exp(\mathrm{i}kz + \mathrm{i}n\theta). \tag{9}$$

The surface under perturbation can be represented as

$$r = 1 + \eta(z, t), \quad \eta = D(t)\exp(\mathrm{i}kz + \mathrm{i}n\theta). \tag{10}$$

Considering the kinematic boundary conditions of Eqs. (4) and (5), the coefficients of potential flow function Eq. (9) can be resolved as

$$A(t) = \frac{D'(t) + [\mathrm{i}U_1(t)k]D(t)}{kI_n'(k)}, \tag{11}$$

$$B(t) = \frac{D'(t)}{kK_n'(k)}. \tag{12}$$

Taking the potential flow functions into the dynamical boundary condition of Eq. (6), it can be written as the form

$$\begin{aligned} I_n(k)&\left[\frac{D''(t) + [\mathrm{i}U_1(t)k]D'(t) + \mathrm{i}kD(t)U_1'(t)}{kI_n'(k)} + \mathrm{i}U_1(t)k\frac{D'(t) + [\mathrm{i}U_1(t)k]D(t)}{kI_n'(k)}\right] - \left[\rho_{21}K_n(k)\frac{D''(t)}{kK_n'(k)}\right] \\ &+ \frac{2}{Re}k^2I_n''(k)\frac{D'(t) + [\mathrm{i}U_1(t)k]D(t)}{kI_n'(k)} - \mu_{21}\frac{2}{Re}k^2K_n''(k)\frac{D'(t)}{kK_n'(k)} \\ &= \frac{1}{We}D(t)(-k^2 - n^2 + 1). \end{aligned} \tag{13}$$

For convenience, Eq. (13) can be simplified and summarized as

$$C_1D''(t) + C_2D'(t) + C_3D(t) = 0, \tag{14}$$

where

$$C_1 = \frac{I_n(k)}{kI_n'(k)} - \frac{\rho_{21}K_n(k)}{kK_n'(k)},$$

$$C_2 = \frac{1}{Re}\left[\frac{2kI_n''(k)}{I_n'(k)} - \frac{2\mu_{21}kK_n''(k)}{K_n'(k)}\right] + \frac{2I_n(k)\mathrm{i}U_1(t)}{I_n'(k)},$$

$$C_3 = \frac{I_n(k)\mathrm{i}U_1'(t)}{I_n'(k)} - \frac{I_n(k)U_1^2(t)k}{I_n'(k)} + \frac{1}{Re}\frac{2k^2I_n''(k)}{I_n'(k)}\mathrm{i}U_1(t) + \frac{1}{We}(k^2 + n^2 - 1).$$

In order to make Eq. (14) easy to be solved, the transformation can be employed to make it as the Hill's equation form,[42,44] i.e.,

$$D(t) = F(t)\exp\left(-\int\frac{1}{2}\frac{C_2}{C_1}dt\right). \tag{15}$$

Consequently, Eq. (14) can be transformed as

$$\frac{d^2F(t)}{dt^2} + F(t)\left(-\frac{1}{2}\frac{C_2'}{C_1} - \frac{1}{4}\frac{C_2^2}{C_1^2} + \frac{C_3}{C_1}\right) = 0, \tag{16}$$

where

$$-\frac{1}{2}\frac{C_2'}{C_1} = -\frac{1}{C_1}\frac{I_n(k)}{I_n'(k)}iU_1'(t),$$

$$\frac{C_3}{C_1} = \frac{1}{C_1}\left[\frac{I_n(k)iU_1'(t)}{I_n'(k)} - \frac{I_n(k)U_1^2(t)k}{I_n'(k)} + \frac{1}{Re}\frac{2k^2I_n''(k)}{I_n'(k)}iU_1(t) + \frac{1}{We}(k^2+n^2-1)\right],$$

$$-\frac{1}{4}\frac{C_2^2}{C_1^2} = -\frac{1}{4C_1^2}\left[\frac{1}{Re}\frac{2kI_n''(k)}{I_n'(k)} - \frac{1}{Re}\frac{2\mu_{21}kK_n''(k)}{K_n'(k)} + \frac{2I_n(k)iU_1(t)}{I_n'(k)}\right]^2.$$

Since the dimensionless basic velocity of the liquid jet is given as $U_1 = 1 + \Delta U\cos(2\tau)$, where $\tau = 0.5\omega_s t$, Eq. (16) can be rewritten as

$$\frac{d^2F(\tau)}{d\tau^2} + F(\tau)[\theta_0 + 2\theta_2\cos(2\tau) + 2\theta_4\cos(4\tau)] = 0, \tag{17}$$

where

$$\theta_0 = \frac{4}{\omega_s^2}\left\{-\frac{1}{4C_1^2}\left(A_1^2 + 2A_1A_2 + A_2^2A_4\right) + \frac{1}{C_1}\left[A_3 - A_4\frac{I_n(k)k}{I_n'(k)} + \frac{1}{Re}\frac{2I_n''(k)k^2}{I_n'(k)}i\right]\right\},$$

$$2\theta_2 = \frac{4}{\omega_s^2}\left\{-\frac{1}{4C_1^2}\left(2A_1A_2\Delta U + 2A_2^2\Delta U\right) + \frac{1}{C_1}\left[-2\frac{I_n(k)k}{I_n'(k)}\Delta U + \frac{1}{Re}\frac{2I_n''(k)k^2}{I_n'(k)}i\Delta U\right]\right\},$$

$$2\theta_4 = \frac{4}{\omega_s^2}\left\{-\frac{1}{4C_1^2}\left(A_2^2\frac{\Delta^2U}{2}\right) + \frac{1}{C_1}\left[-\frac{\Delta^2U}{2}\frac{I_n(k)k}{I_n'(k)}\right]\right\},$$

$$A_1 = \frac{1}{Re}\frac{2kI_n''(k)}{I_n'(k)} - \frac{1}{Re}\frac{2\mu_{21}kK_n''(k)}{K_n'(k)}, \quad A_2 = \frac{2I_n(k)i}{I_n'(k)},$$

$$A_3 = \frac{1}{We}(k^2+n^2-1), \quad A_4 = 1 + \frac{\Delta^2U}{2}.$$

According to the Floquet theory,[44] the solution of Eq. (17) has the following form:

$$F(\tau) = \exp(\beta\tau)\varphi(\tau), \tag{18}$$

where

$$\cosh(\pi\beta) = 1 - 2\sin^2\left(\frac{\pi\theta_0^{1/2}}{2}\right) - \pi\left(\frac{\theta_2^2}{1-\theta_0} + \frac{\theta_4^2}{2^2-\theta_0}\right)\sin\left(\pi\theta_0^{1/2}\right)\frac{1}{4\theta_0{}^{1/2}}.$$

To obtain the temporal growth rate of the disturbance wave, the displacement of surface perturbation can be rewritten as

$$\eta(x,t) = D(t)e^{ikz+in\theta} = F(\tau)e^{-\int\frac{C_2}{2C_1}dt}e^{(ikz+in\theta)} = \varphi(0.5\omega_s t)e^{\omega t}e^{(ikz+in\theta)}, \tag{19}$$

where the complex frequency of perturbation is represented by $\omega = \left[\beta(0.5\omega_s t) - \int\frac{C_2}{2C_1}dt\right]$. The real part of ω (denoted by ω_r) stands for the temporal growth rate and the imaginary part of ω (denoted by ω_i) denotes the perturbation frequency, respectively. Therefore, the temporal growth rate of the disturbance wave can be represented as

$$\omega_r = \text{Real}\left[\beta(0.5\omega_s) - \frac{C_2}{2C_1}\right] = 0.5\omega_s\text{Real}(\beta) - \frac{1}{Re}\frac{k^2[I_n''(k)K_n'(k) - \mu_{21}K_n''(k)I_n'(k)]}{I_n(k)K_n'(k) - \rho_{21}K_n(k)I_n'(k)}, \tag{20}$$

where

$$\beta = \frac{1}{\pi}\text{arccosh}\left[1 - 2\sin^2\left(\frac{\pi\theta_0^{1/2}}{2}\right) - \pi\left(\frac{\theta_2^2}{1-\theta_0} + \frac{\theta_4^2}{2^2-\theta_0}\right) \times \sin\left(\pi\theta_0^{1/2}\right)\frac{1}{4\theta_0{}^{1/2}}\right].$$

C. Validation

The dispersion relation of Eq. (20) can be validated by comparing it with previous studies. Figure 2(a) shows the comparison between results obtained by Eq. (20) and the dispersion relation derived by Funada *et al.*,[54] considering the development of axisymmetric disturbance $n = 0$ under different Weber numbers. The dispersion relation in Funada *et al.* is derived from the viscous potential theory without considering velocity modulation. Therefore, results of the present work shown in Fig. 2(a) are all calculated by setting $\Delta U = 0$. It is observed that a good agreement can be reached between our results and those of Funada *et al.* as *We* gradually changes. For the non-axisymmetric cases with $n = 1$, our results are validated with those in Yang,[55] as shown in Fig. 2(b). The dispersion relation in his work is obtained by the Euler equation without considering velocity modulation. As a consequence, our results given in Fig. 2(b) are all calculated by setting $\Delta U = 0$ and $Re \to \infty$. It is observed that with the variation of *We*, a good agreement can be reached invariably between our results and those of Yang.

III. RESULTS AND DISCUSSION

To study the effects of various parameters on the instability of the liquid jet, a reference state must be given first. In this work, the diameter of the jet is considered on the order of $\sim 10^{-3}$ m, and the jet average velocity is approximately ~ 10 m/s. As a consequence, the characteristic frequency of the jet is on the order of $\sim 10^4$ Hz. Considering the common fluid combination such as water jet in an air environment, the densities of liquid jet and gas surroundings are on the order of $\sim 10^3$ and ~ 1 kg/m^3, and the dynamical viscosities of liquid jet and gas surroundings are on the order of $\sim 10^{-3}$ and $\sim 10^{-5}$ Pas, respectively. Without loss of generality, the typical values of dimensionless parameters for the reference state can be chosen as

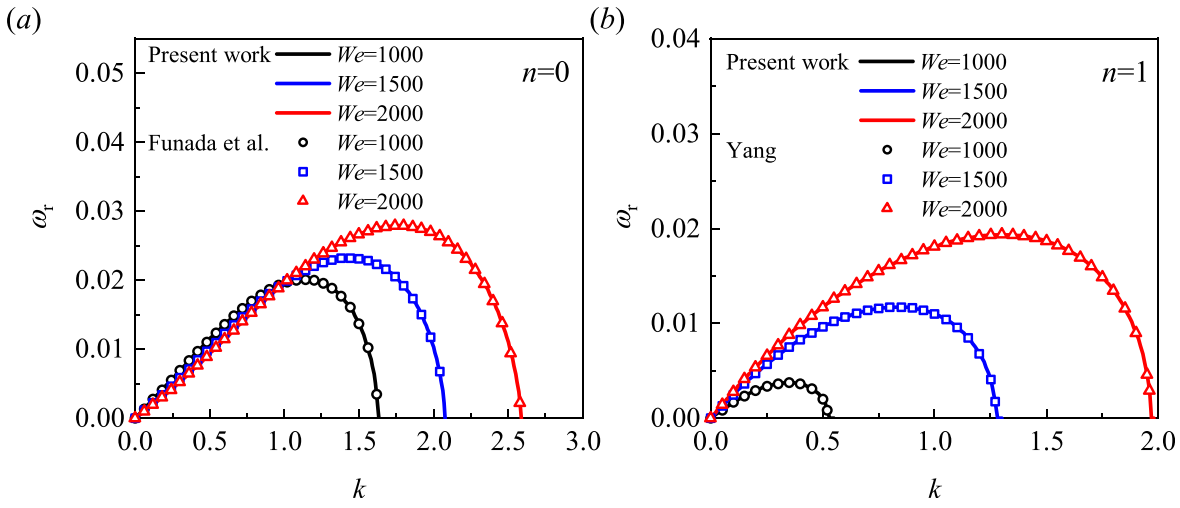

FIG. 2. Comparison between the results obtained from Eq. (20) (solid lines) with (a) Funada *et al.*[54] (hollow symbols) and (b) Yang[55] (hollow symbols). The parameters are unified at (a) $Re = 1000$, $We = 1000$ (black line and circles), 1500 (blue line and squares), 2000 (red line and triangles), $\rho_{21} = 0.0013$, $\Delta U = 0$, $n = 0$, and (b) $Re \to \infty$, $We = 1000$ (black line and circles), 1500 (blue line and squares), 2000 (red line and triangles), $\rho_{21} = 0.0013$, $\Delta U = 0$, $n = 1$, respectively.

$$\rho_{21} = 0.001, \quad \mu_{21} = 0.01, \quad Re = 5000,$$
$$We = 5000, \quad \Delta U = 0.6, \quad \omega_s = 1.5.$$

It is notable that the Weber number defined with the gas phase (i.e., $We_g = We \times \rho_{21}$) equals to a specifical value of 5, indicating that the breakup of a liquid jet under the reference state is at the first wind-induced regime according to the classification criterion summarized by Lin and Reitz.[10] We analyze the effects of control parameters (ΔU, ω_s, We, and Re) on the temporal instability of the liquid jet, considering both the axisymmetric disturbance ($n = 0$) and non-axisymmetric disturbances with different azimuthal wavenumbers ($n = 1$–3). The mode competition will also be analyzed by comparing the maximum growth rates of different azimuthal modes, where the predominant instability mode can be determined.

A. Effect of the velocity oscillation amplitude ΔU

The influence of longitudinal perturbation on the inlet velocity of the liquid jet is directly reflected by the velocity oscillation amplitude ΔU. Figure 3 represents the effect of ΔU on the jet instability under axisymmetric disturbance and non-axisymmetric disturbances. For the axisymmetric disturbance with $n = 0$, as shown in Fig. 3(a), it is observed that only one unstable wavenumber region with $\omega_r > 0$ can be observed if the velocity oscillation is absent or at a relatively small value (e.g., $\Delta U = 0$ and 0.2). As the cutoff wavenumber (denoted by k_c) and the most unstable wavenumber [denoted by k_d, which corresponds to the maximum growth rate MAX(ω_r)] range on the order of $\sim O(1)$, the jet instability is supposed to be induced by the combination of the RPI and KHI. Therefore, this unstable parameter zone is defined as the RP-KHI region. With the increase in velocity oscillation amplitude (e.g., $\Delta U = 0.6$ and 1.0), it is found that more unstable wavenumber regions are triggered in the short-wavelength regions with $k \sim O(10)$, suggesting that the KHI plays a significant effect on these wavenumber regions. We define these regions as oscillating Kelvin–Helmholtz instability (OKHI) regions. It is notable that the occurrence of OKHI regions is also observed in situations where the liquid jet with uniform velocity is driven by the co-flowing gas with periodic velocity oscillation.[44] A continuous increase in ΔU (e.g., $=1.8$) can lead to another OKHI region at a larger wavenumber; however, the growth rate of this region is much smaller than that of the first OKHI region. It has been indicated in previous studies that the first and the second OKHI regions correspond to the sub-harmonic and the harmonic characteristics of the perturbation wave, respectively.[44,56] Comparing the results under different ΔU, it is found that both the RP-KHI and OKHI regions widen with the increase in ΔU, indicating that the velocity modulation brings more perturbation waves into jet instability. For the RP-KHI and the OKHI regions, the growth rates increase with ΔU increasing. Moreover, the maximum growth rate of the OKHI region will become larger than that of the RP-KH region as ΔU gradually increases, indicating that the physical mechanisms of jet instability transfer from RP-KHI to OKHI. As a consequence, the short-wavelength perturbation waves grow faster than those of the long-wavelength perturbation waves, resulting in a smaller size of the droplets. This tendency is similar with that observed in numerical simulations.[50] Figure 3(b) shows the growth rate curves for the non-axisymmetric disturbance with $n = 1$. Overall, the results of perturbation development with $n = 1$ are similar to those with $n = 0$. The perturbation growth rates of non-axisymmetric disturbances with azimuthal wavenumber $n = 2$ are shown in Fig. 3(c). Different from the situations of $n = 0$ and 1, it is observed that the disturbance whose wavelength tends to be infinite (i.e., $k \approx 0$) becomes stable as the growth rate is less than zero. This is due to the fact that the RPI cannot trigger the unstable mode in long-wavelength region for high azimuthal wavenumbers.[57] As for the RP-KHI and OKHI regions, the growth rate increases with the increase in ΔU. Figure 3(d) represents the perturbation growth rate of non-axisymmetric disturbances with azimuthal wavenumber $n = 3$, in which the unstable perturbations only occur as ΔU increases large enough (e.g., $\Delta U \geq 0.6$). It is found that the OKHI region dominates the jet instability invariably, and the RP-KH region only occurs when the velocity oscillation amplitude is relatively high (i.e., $\Delta U = 1.8$).

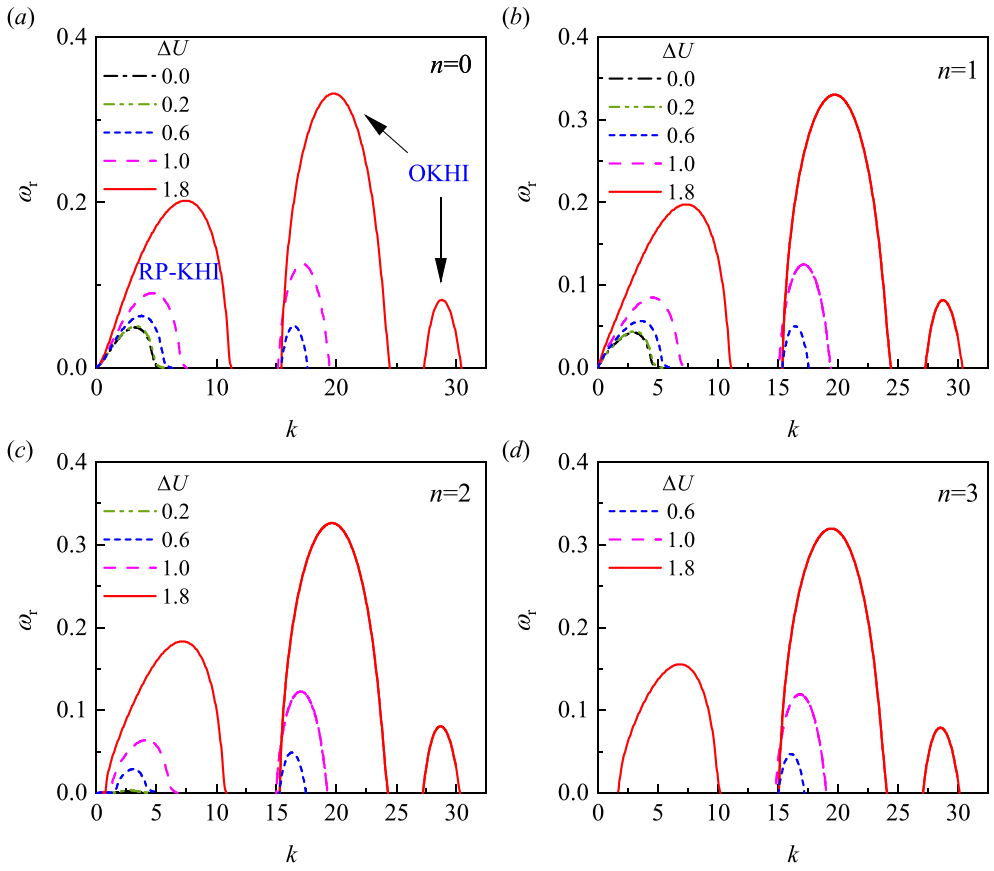

FIG. 3. Perturbation growth rates ω_r vs wavenumbers k as the velocity oscillation amplitude ΔU changes, where (a)–(d) denote the circumferential perturbations with azimuthal wavenumbers of $n = 0$, 1, 2 and 3, respectively.

As the perturbation wave with the maximum growth rate dominates the jet breakup, we further analyze the variation of the maximum growth rate [MAX(ω_r)] and the corresponding most unstable wavenumber (k_d) with ΔU. The results are given in Figs. 4(a) and 4(b), respectively. Figure 4(a) shows that the maximum growth rate of perturbation with disturbance $n = 0$ and $n = 1$ will increase with the increase in ΔU. Specifically, once ΔU exceeds a critical value of 0.7, the occurred positions of maximum growth rate will transfer from the

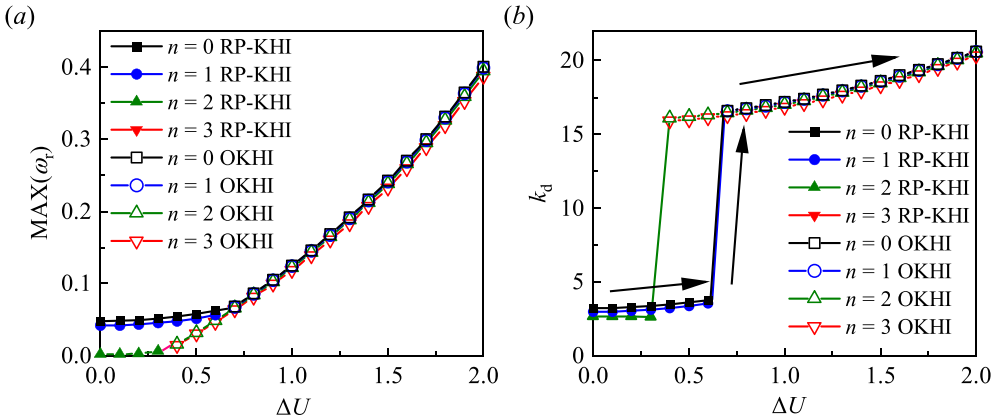

FIG. 4. Effects of the velocity perturbation amplitude ΔU on (a) the maximum growth rate MAX(ω_r) and (b) the most unstable wavenumber k_d. Arrows in (b) represent the variation of the most unstable wavenumber of the predominate mode as ΔU increases.

RP-KHI region (denoted by the solid symbols) to the OKHI region (denoted by the hollow symbols). The values of maximum growth rates in the RP-KHI region for $n = 0$ are slightly larger than those for $n = 1$, whereas the values of maximum growth rates in the OKHI region for $n = 1$ are almost the same as those for $n = 0$. For the non-axisymmetric disturbances with $n = 2$ and $n = 3$, the values of the maximum growth rates of these two unstable modes are almost equal under different values of ΔU. Specifically, when $\Delta U \leq 0.3$, the occurred positions of maximum growth rate are within the RP-KHI region. Once $\Delta U \geq 0.4$, the maximum growth rate occurs within the OKHI region. Generally, the azimuthal mode corresponding to the maximum value of MAX(ω_r) dominates the jet breakup, which is considered as the predominant mode. Therefore, the predominant mode can be identified by comparing the values of MAX(ω_r) for different n. Figure 4(a) indicates that the axisymmetric mode maintains the predominant mode under a relatively low value of ΔU. With the increase in ΔU (i.e., $\Delta U \geq 0.7$), the maximum growth rates of modes $n = 0$–3 have little difference, indicating that these modes act jointly to induce the jet instability in the OKHI region. The effect of ΔU on the most unstable wavenumber of the predominant mode under different n is shown in Fig. 4(b). For each mode, the transition from the RP-KHI region to the OKHI region by increasing ΔU can make the most unstable wavenumber transfer from the long-wavelength region to the short-wavelength region. With the increase in ΔU, the most unstable wavenumber of the predominant mode will increase along the arrows sketched in Fig. 4(b), which means that the droplets generated after jet breakup become smaller. Overall, the increase in velocity oscillation amplitude can improve the efficiency of liquid jet breakup.

B. Effect of the velocity oscillation frequency ω_s

Figure 5 represents the effect of velocity oscillation frequency ω_s on the jet instability for both axisymmetric disturbance and non-axisymmetric disturbances with different azimuthal wavenumbers. The perturbation growth rate curves for the axisymmetric disturbance $n = 0$ are given in Fig. 5(a). When the oscillation frequency is relatively high (e.g., $\omega_s = 0.50, 1.00, 1.50, 2.00$), the RP-KHI and OKHI regions are located at two separated crests. Specifically, the curves in the RP-KHI region have little difference as ω_s changes, whereas those in the OKHI region shift to low wavenumber with ω_s decreasing. Moreover, the maximum growth rate of the OKHI region increases significantly with the decrease in ω_s. The variation tendency of the OKHI region with ω_s is sketched clearly by the arrow in Fig. 5(a). With the continuous decrease in ω_s (e.g., $\omega_s = 0.1$), the OKHI region gradually intersects with the RP-KHI region, indicating a complex competition between different instability mechanisms. More wave crests related to OKHI can also be observed at the growth rate curve. Figures 5(b) and 5(c) show the perturbation growth rate curves for the non-axisymmetric perturbation with $n = 1$ and 2, respectively. Overall, the variation

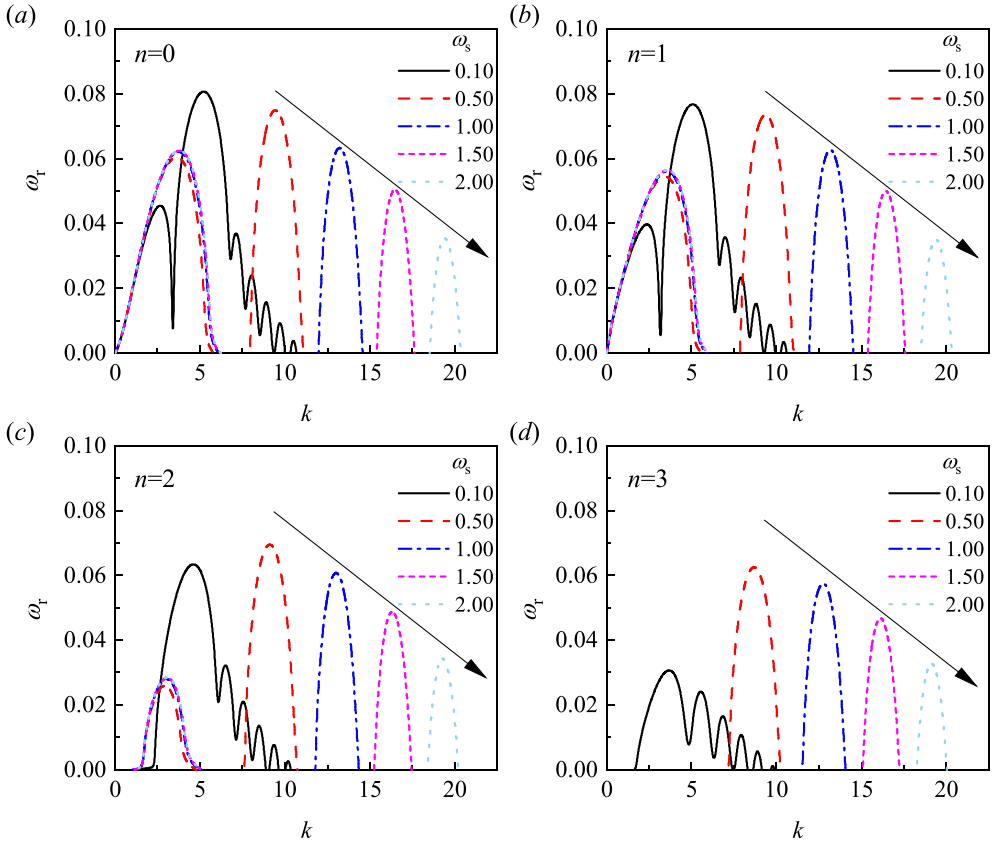

FIG. 5. Perturbation growth rates ω_r vs wavenumbers k as the velocity oscillation frequency ω_s changes, where (a)–(d) denote the circumferential perturbations with azimuthal wavenumbers of $n = 0$, 1, 2 and 3, respectively.

tendencies of the growth rate curves under different ω_s are quite similar to those of the axisymmetric cases, but with smaller specifical values. The non-axisymmetric perturbation growth rate curves with $n = 3$ are a bit different from those of $n = 0$–2, as shown in Fig. 5(d). It is observed that the RP-KHI region vanishes, and only the unstable growth rate curves within the OKHI region exist.

Figure 6 displays the effects of velocity oscillation frequency MAX(ω_r) on the maximum growth rate MAX(ω_r) and the corresponding most unstable wavenumber k_d, respectively. Figure 6(a) shows that the maximum growth rate for both the axisymmetric and the non-axisymmetric perturbations will first increase and then decrease with the increase in ω_s. For each mode, the occurred position of maximum growth rate will transfer from the OKHI region (hollow symbols) to the RP-KHI region (solid symbols) as ω_s gradually increases. Once the oscillation frequency is at relatively high or low values [e.g., $\omega_s \sim O(10^1)$ or $\sim O(10^{-3})$], the maximum growth rate maintains almost constant, indicating that the velocity oscillations with high or low frequencies only have little influence on jet instability. This can be explained from the physical perspective that the extra volume of fluid brought by velocity oscillation decreases as ω_s increases under certain oscillation amplitude. Therefore, the jet instability is decided by its intrinsic RP-KHI under high ω_s. However, the extra volume of fluid brought by velocity oscillation increases significantly under low ω_s, indicating that the velocity oscillation plays a more significant role than the intrinsic RP-KHI, thus the jet instability is dominated by OKHI. Comparing the values of MAX(ω_r) of different modes, it is found that the axisymmetric mode with $n = 0$ maintains the predominate mode invariably. The effect of ω_s on the most unstable wavenumber k_d is shown in Fig. 6(b). For modes $n = 0$–2, the most unstable wavenumber will first increase and then decrease with the increase in ω_s, which is caused by the transition of most unstable wavenumber region from OKHI region to RP-KH region. As k_d occurs in the OKHI region invariably for $n = 3$, the value of k_d keeps increasing with ω_s. The variation route of k_d for the predominate mode is also plotted by the arrows, showing the increasing tendency first and then the decreasing tendency with the increase in ω_s. Therefore, the resulting droplet size is relatively large under high or low oscillation frequencies but decreases significantly as $\omega_s \sim O(10^0)$.

C. Effect of the Weber number *We*

The Weber number *We* represents the relative importance between the inertial stress and the surface tension. Figure 7 shows the growth rate curves as the value of *We* gradually changes from $O(10^2)$ to $O(10^4)$. For the axisymmetric mode with $n = 0$ [see Fig. 7(a)], it is found that the jet instability is dominated by RPI under relatively small *We* (e.g., $We = 100$) as the cutoff wavenumber is very close to 1, indicating that the breakup of the liquid jet is mainly induced by surface tension. With the increase in *We* (e.g., $We = 1000$, 5000, and 10 000), the surface tension is weakened, and the velocity difference between the liquid jet and the gas environment plays a more significant role, leading to the occurrence of RP-KHI region and the OKHI region. With the increase in *We*, the unstable wavenumber regions of both RP-KHI and OKHI are widened, indicating that the decrease in surface tension brings more perturbation waves into jet instability. For the OKHI region, the increase in *We* leads to an increase in the maximum perturbation growth rate, and the unstable wavenumber region will be shifted to a shorter wavelength (larger *k*). For the non-axisymmetric disturbance with $n = 1$–3, as shown in Figs. 7(b), 7(c), and 7(d), respectively, it is found that the unstable perturbation waves cannot be triggered under low Weber number (e.g., $We = 100$). This observation is consistent with the previous work, which indicates that the surface tension can suppress the non-axisymmetric disturbances. For the non-axisymmetric modes $n = 1$–3, the increase in *We* leads to widened unstable perturbation regions, both for RP-KHI and OKHI, and the growth rate increases significantly with *We* increasing.

Figure 8 displays the effects of Weber number *We* on the maximum growth rate MAX(ω_r) and the most unstable wavenumber k_d, respectively. For the axisymmetric disturbance with $n = 0$, as shown in Fig. 8(a), the increase in *We* will first decrease and then increase the maximum growth rate of the perturbation due to the transition of instability mechanisms from almost pure RPI to RP-KHI as *We* gradually increases at the order of $We \sim 10^2$ to $\sim 10^3$. It is notable that the RP-KHI will always dominate the instability of axisymmetric mode with the variation of *We*. As for the non-axisymmetric disturbance $n = 1$–3, the increase in *We* can enhance the jet instability invariably. Moreover, with the increase in *We*, the occurred positions of maximum growth rate will transfer from the OKHI region (hollow

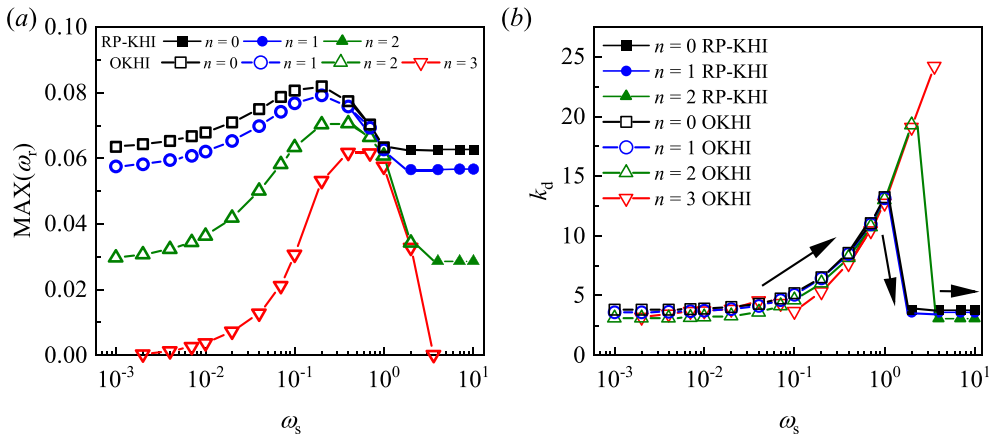

FIG. 6. Effects of the velocity oscillation frequency ω_s on (a) the maximum growth rate MAX(ω_r) and (b) the most unstable wavenumber k_d. Arrows in (b) represent the variation of the most unstable wavenumber of the predominate mode as ω_s increases.

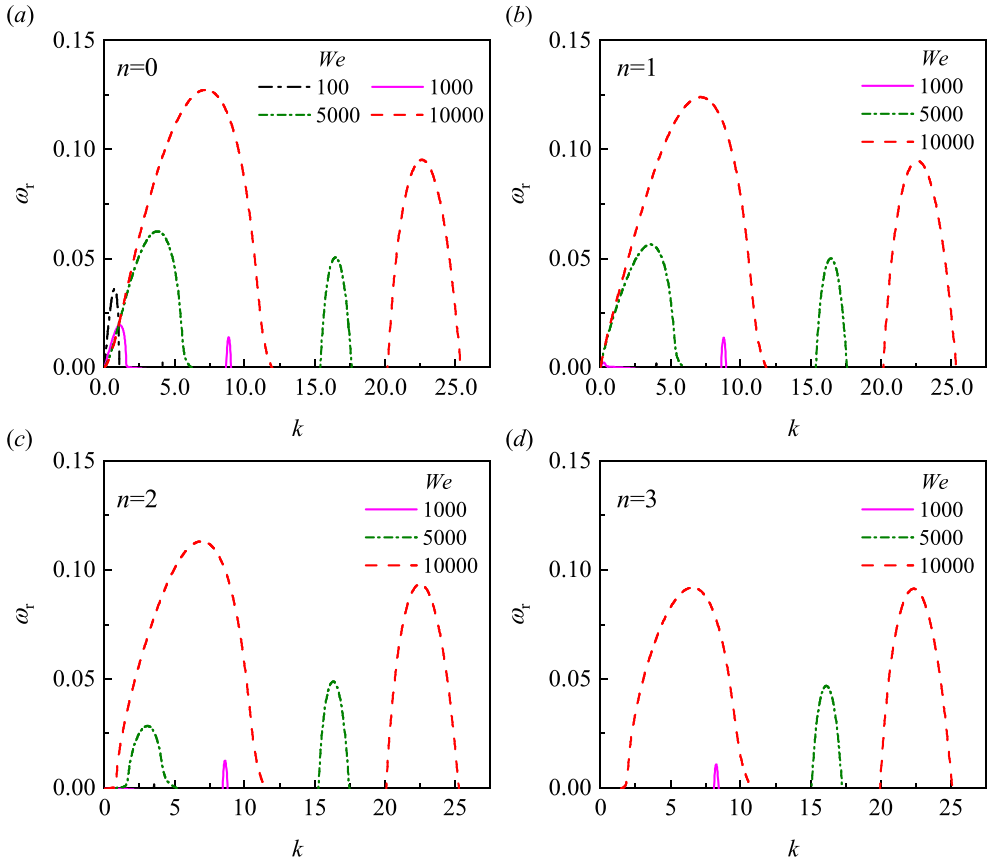

FIG. 7. Perturbation growth rates ω_r vs wavenumbers k as We changes, where (a)–(d) denote the circumferential perturbations with azimuthal wavenumbers of $n = 0$, 1, 2 and 3, respectively.

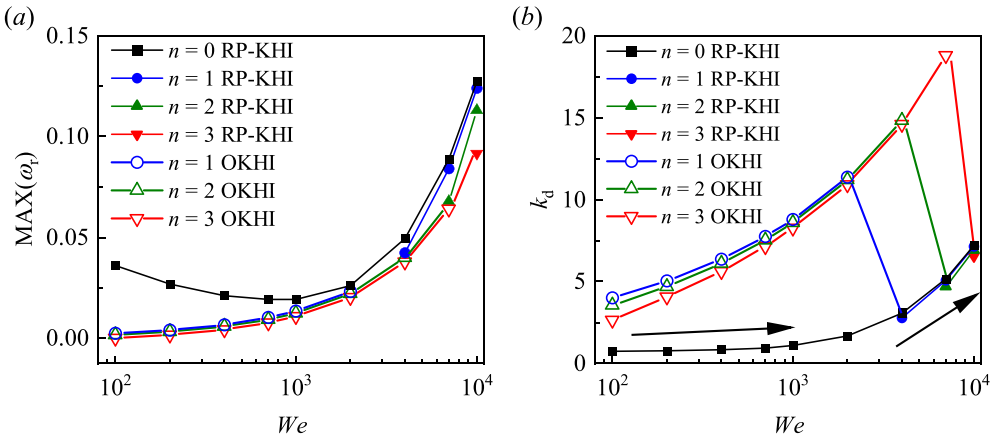

FIG. 8. Effects of the Weber number We on (a) the maximum growth rate MAX(ω_r) and (b) the most unstable wavenumber k_d. Arrows in (b) represent the variation of the most unstable wavenumber of the predominate mode as We increases.

symbols) to the RP-KHI region (solid symbols). Once the Weber number is relatively high (e.g., $We > 7000$), the maximum growth rate of non-axisymmetric disturbance with $n = 1$ can almost be equal to that of axisymmetric disturbance with $n = 0$, indicating that the jet instability will be determined by the competition between axisymmetric and non-axisymmetric disturbances. The variations of the most unstable wavenumber k_d under different We are represented in Fig. 8(b). It is clear that the increase in the We will increase the most

unstable wavenumber continuously for the axisymmetric disturbance ($n = 0$). For the non-axisymmetric modes $n = 1$–3, the most unstable wavenumber will first increase, then decrease, and finally increase with the increase in *We*, which is caused by the transition of physical mechanisms from OKHI to RP-KHI. The arrows in Fig. 8(b) represent the variation route of the most unstable wavenumber for the predominate mode. As the axisymmetric disturbance dominates the jet breakup, the value of k_d for the predominate mode keeps increasing with *We*, indicating that a decrease in surface tension can result in smaller droplets.

D. Effect of the Reynolds number *Re*

The effect of fluid viscosities on the jet instability is investigated by changing the Reynolds number *Re* from $O(10^2)$ to $O(10^5)$, and the results are given in Fig. 9. Figure 9(a) shows the growth rate curves of the axisymmetric mode with $n = 0$ as *Re* gradually increases. The increase in *Re* can enhance the instability of the RP-KHI region as the viscous dissipation effect is weakened, and the growth rate curves of the RP-KHI region almost converge as *Re* increases over 5000. The OKHI region also occurs as *Re* gradually increases (e.g., $Re \geq 5000$), and the increase in *Re* can enhance the growth rate of OKHI. It is notable that the variation of *Re* almost has no influence on the wavenumber range of the OKHI region. The growth rate curves of liquid jets with non-axisymmetric disturbances with $n = 1$ and 2 under different Reynolds numbers are shown in Figs. 9(b) and 9(c), respectively. Similar to the situation of $n = 0$, the growth rates of both RP-KHI and OKHI regions can be increased by the decrease in *Re*. For the non-axisymmetric disturbance with $n = 3$, as shown in Fig. 9(d), the RP-KHI region vanishes, and the instability of the OKHI region only occurs as *Re* increases to large values (e.g., $Re \geq 5000$).

Figure 10 represents the effects of viscosity on the maximum growth rate MAX(ω_r) and the most unstable wavenumber k_d, respectively. As shown in Fig. 10(a), the maximum growth rate of the axisymmetric mode can be enhanced by increasing the Reynolds number, and the most unstable wavenumber region will gradually shift from the RP-KHI region to the OKHI region. As for the non-axisymmetric disturbance with $n = 1$ and $n = 2$, similar variation tendencies can be observed as *Re* gradually increases. The non-axisymmetric disturbance with $n = 3$ becomes unstable as *Re* increases over a critical value around $Re \approx 2000$, with its growth rate increasing with the increase in *Re*. The variations of the most unstable wavenumber k_d under different Reynolds numbers are shown in Fig. 10(b). The variation of *Re* only affects the values of k_d slightly within the parametric range of both RP-KHI and OKHI but leads to the sudden increase in k_d as the instability mechanism converts from RP-KHI to OKHI. As for the predominate mode, the value of k_d changes according to the route sketched in Fig. 10(b), indicating that the droplet size decreases significantly as *Re* exceeds the critical value of 10^4.

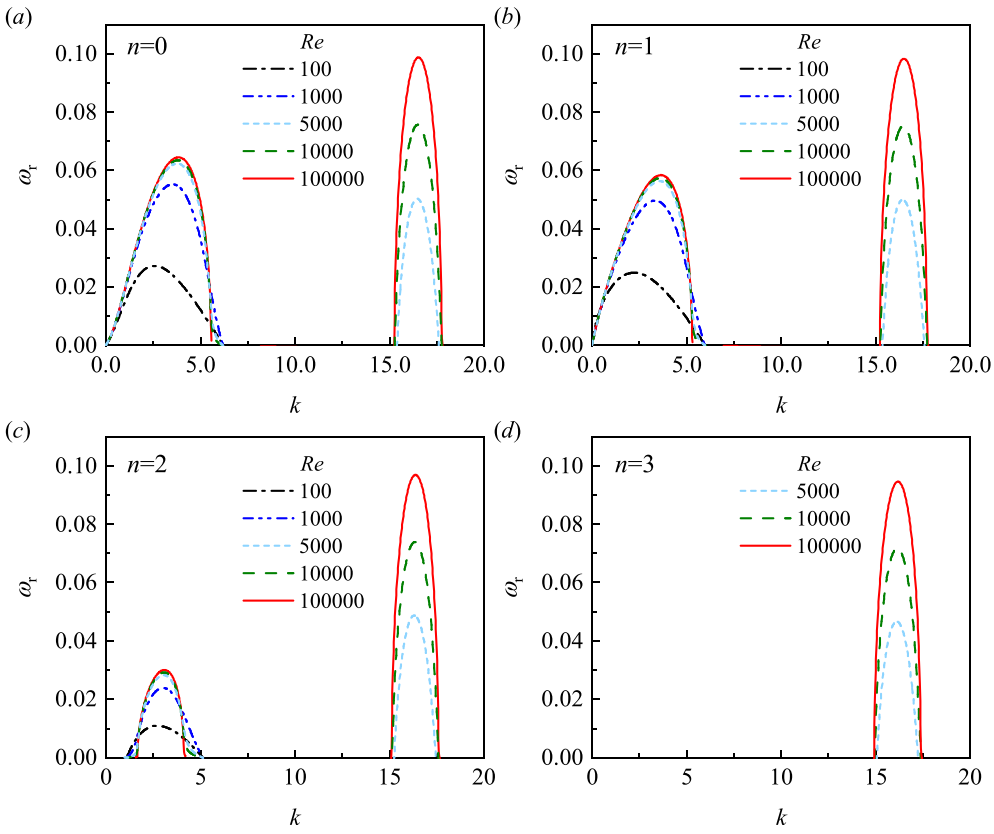

FIG. 9. Perturbation growth rates ω_r vs wavenumbers *k* as *Re* changes, where (a)–(d) denote circumferential perturbations with azimuthal wavenumbers of $n = 0$, 1, 2 and 3, respectively.

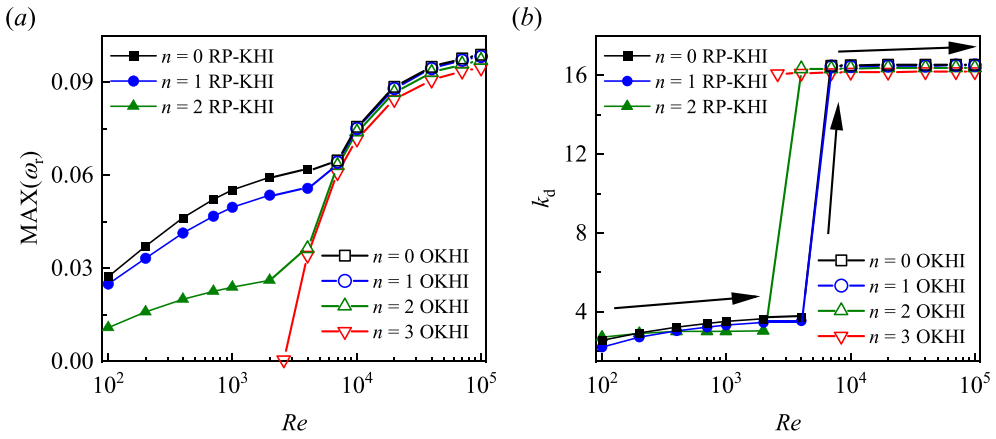

FIG. 10. Effects of the Reynolds number *Re* on (a) the maximum growth rate MAX(ω_r) and (b) the most unstable wavenumber k_d. Arrows in (b) represent the variation of the most unstable wavenumber of the predominate mode as *Re* increases.

E. Transition of the predominate mode

In order to represent the predominate mode transition of jet instability under velocity modulation more clearly, the phase diagrams of the predominate modes as the velocity oscillation amplitude ΔU and frequency ω_s vary is given in Fig. 11. As shown in Figs. 4 and 6, the jet instability is dominated by RP-KHI of the axisymmetric mode with $n = 0$ under relatively low ΔU or high ω_s; while the increase in ΔU or the decrease in ω_s can lead to the jet instability in OKHI region, and the OKHI under different azimuthal wavenumbers n can compete intensely to the affect the jet breakup. Therefore, two categories of predominate modes are defined in Fig. 11, i.e., the RP-KHI mode with $n = 0$ and the OKHI mode. It is observed in Fig. 11 that the jet instability maintains the RP-KHI mode invariably if the velocity oscillation amplitude ΔU is lower than a critical value around 0.3. Below this critical amplitude, the velocity oscillation is too weak to dominate the jet instability. With the increase in ΔU, the critical value of ω_s, which leads to mode transition, also increases correspondingly. This can be explained qualitatively in the following: the increase in ω_s leads to a shorter velocity oscillation period and thus smaller volume of the additional liquid brought by the oscillation; therefore, a larger amplitude ΔU is needed to trigger the predominate mode transition from RP-KHI to OKHI. Moreover, the transition boundary for these two physical mechanism regimes can be approximated by a linear relationship (see the dashed line in Fig. 11).

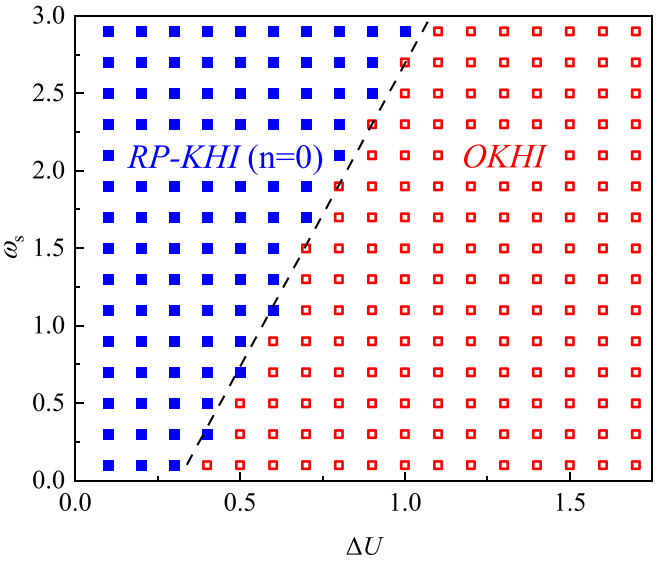

FIG. 11. Phase diagram of the predominate mode in (ΔU, ω_s) space.

IV. CONCLUSION

The temporal linear instability of viscous liquid jets under periodic velocity oscillation is studied, considering the development of both axisymmetric and non-axisymmetric perturbations. Utilizing the viscous potential theory and the Floquet theory, an analytical dispersion relation of perturbation growth rate is deduced. The dispersion relation derived in this work is validated by comparing it with the previous results, ignoring the velocity modulation on the basic flow. The effects of dimensionless control parameters (the oscillation amplitude ΔU and frequency ω_s, the Weber number *We*, and the Reynolds number *Re*) are investigated through a parametric study, in which the variations of the maximum growth rate MAX(ω_r) and the corresponding most unstable wavenumber k_d are summarized for the unstable modes with different azimuthal wavenumbers. It is found that the velocity oscillation can trigger several unstable wavenumber regions with short wavelengths, which is related to the OKHI. The OKHI competes with the intrinsic RP-KHI to modulate the jet breakup. With the increase in ΔU, the maximum growth rate of the OKHI region gradually overtakes that of the RP-KHI region, indicating the transition of the jet instability mechanism. The increase in ω_s results in the OKHI region with shorter wavelength and smaller growth rates, while the growth rate curves of RP-KHI region are insensitive to ω_s. Therefore, the maximum growth rate of the RP-KHI region exceeds that of the OKHI region with the increase in ω_s. The perturbation growth under relatively high and low frequency ranges also converges to constant values. The increase in *We* can first suppress and then enhance the growth rate of RP-KHI but enhance that of OKHI continuously, and the jet instability is dominated invariably by the RP-KHI of the axisymmetric

mode. Increasing the *Re* will enhance the instability of both the RP-KHI region and the OKHI region. However, the variation of *Re* hardly affects the unstable wavenumber regions. Choosing ΔU and ω_s as the characteristic parameters, the phase diagram of the predominate mode is identified, which reveals that the transition boundary between RP-KHI and OKHI can be approximated as a straight line. This study is supposed to give some theoretical guidance on the modulation of jet instability in industrial fields.

ACKNOWLEDGMENTS

This work was supported by the National Natural Science Foundation of China (Grant Nos. 12027801, 11902318, 12272372, 12202437, and 12388101), the Youth Innovation Promotion Association CAS (Grant Nos. 2018491 and 2023477), and the Fundamental Research Funds for the Central Universities.

AUTHOR DECLARATIONS

Conflict of Interest

The authors have no conflicts to disclose.

Author Contributions

Ran Qiao: Data curation (equal); Formal analysis (equal); Investigation (equal); Methodology (equal); Writing – original draft (equal). **Chengxi Zhao:** Data curation (equal); Software (equal); Validation (equal); Visualization (equal). **Zhaodong Ding:** Resources (equal); Software (equal); Validation (equal); Visualization (equal). **Kai Mu:** Conceptualization (lead); Funding acquisition (equal); Resources (equal); Supervision (equal); Writing – review & editing (equal). **Ting Si:** Conceptualization (equal); Funding acquisition (equal); Project administration (equal); Supervision (equal); Writing – review & editing (equal).

DATA AVAILABILITY

The data that support the findings of this study are available from the corresponding author upon reasonable request.

REFERENCES

[1]N. Ashgriz, *Handbook of Atomization and Sprays: Theory and Applications* (Springer Science & Business Media, 2011).
[2]A. H. Lefebvre and V. G. McDonell, *Atomization and Sprays* (CRC Press, 2017).
[3]T. C. Lieuwen, *Unsteady Combustor Physics* (Cambridge University Press, 2021).
[4]M. Bruening and D. Dotzauer, "Just spray it," Nat. Mater. **8**, 449–450 (2009).
[5]A. S. M. Ang and C. C. Berndt, "A review of testing methods for thermal spray coatings," Int. Mater. Rev. **59**, 179–223 (2014).
[6]N. Espallargas, *Future Development of Thermal Spray Coatings: Types, Designs, Manufacture and Applications* (Elsevier, 2015).
[7]G. Matthews, R. Bateman, and P. Miller, *Pesticide Application Methods* (John Wiley & Sons, 2014).
[8]S. Xue, X. Xi, Z. Lan, R. Wen, and X. Ma, "Longitudinal drift behaviors and spatial transport efficiency for spraying pesticide droplets," Int. J. Heat Mass Transfer **177**, 121516 (2021).
[9]R. D. Reitz, "Mechanism of breakup of round liquid jets," in *Encyclopedia of Fluid Mechanics* (Gulf Publishing Company, 1986).
[10]S. P. Lin and R. D. Reitz, "Drop and spray formation from a liquid jet," Annu. Rev. Fluid Mech. **30**, 85–105 (1998).
[11]J. Plateau, *Experimental and Theoretical Statics of Liquids Subject to Molecular Forces Only* (Gauthier-Villars, 1873).
[12]L. Rayleigh, "On the instability of jets," Proc. London Math. Soc. **s1-10**, 4–13 (1878).
[13]L. Rayleigh, "On the instability of a cylinder of viscous liquid under capillary force," London, Edinburgh, Dublin Philos. Mag. J. Sci. **34**, 145–154 (1892).
[14]J. W. Hoyt and J. Taylor, "Waves on water jets," J. Fluid Mech. **83**, 119–127 (1977).
[15]J. Taylor and J. Hoyt, "Water jet photography–techniques and methods," Exp. Fluids **1**, 113–120 (1983).
[16]R. W. Fenn, III and S. Middleman, "Newtonian jet stability: The role of air resistance," AIChE J. **15**, 379–383 (1969).
[17]R. E. Phinney, "The breakup of a turbulent liquid jet in a gaseous atmosphere," J. Fluid Mech. **60**, 689–701 (1973).
[18]J. Portillo, S. Collicott, and G. Blaisdell, "Measurements of axial instability waves in the near exit region of a high speed liquid jet," Phys. Fluids **23**, 124105 (2011).
[19]C. Gong, M. Yang, C. Kang, and Y. Wang, "The acquisition and measurement of surface waves of high-speed liquid jets," J. Vis. **19**, 211–224 (2016).
[20]A. Roth, D. Frantz, W. Chaze, A. Corber, and E. Berrocal, "High-speed imaging database of water jet disintegration Part I: Quantitative imaging using liquid laser-induced fluorescence," Int. J. Multiphase Flow **145**, 103641 (2021).
[21]W. Bo, X. Liu, J. Glimm, and X. Li, "A robust front tracking method: Verification and application to simulation of the primary breakup of a liquid jet," SIAM J. Sci. Comput. **33**, 1505–1524 (2011).
[22]L. Bravo, D. Kim, F. Ham, C. Powell, and A. Kastengren, "Effects of fuel viscosity on the primary breakup dynamics of a high-speed liquid jet with comparison to x-ray radiography," Proc. Combust. Inst. **37**, 3245–3253 (2019).
[23]A. Arote, M. Bade, and J. Banerjee, "Numerical investigations on stability of the spatially oscillating planar two-phase liquid jet in a quiescent atmosphere," Phys. Fluids **31**, 112103 (2019).
[24]M. Fathi, S. Hickel, and D. Roekaerts, "Large eddy simulations of reacting and non-reacting transcritical fuel sprays using multiphase thermodynamics," Phys. Fluids **34**, 085131 (2022).
[25]J. C. Lasheras and E. Hopfinger, "Liquid jet instability and atomization in a coaxial gas stream," Annu. Rev. Fluid Mech. **32**, 275–308 (2000).
[26]A. Zandian, W. Sirignano, and F. Hussain, "Vorticity dynamics in a spatially developing liquid jet inside a co-flowing gas," J. Fluid Mech. **877**, 429–470 (2019).
[27]G. Li, X. Luo, T. Si, and R. X. Xu, "Temporal instability of coflowing liquid-gas jets under an electric field," Phys. Fluids **26**, 054101 (2014).
[28]D. Deshawar and P. Chokshi, "Stability analysis of a thinning electrified jet under nonisothermal conditions," Phys. Rev. E **103**, 023107 (2021).
[29]H. Liu, Z. Wang, L. Gao, Y. Huang, H. Tang, X. Zhao, and W. Deng, "Optofluidic resonance of a transparent liquid jet excited by a continuous wave laser," Phys. Rev. Lett. **127**, 244502 (2021).
[30]Y. Zhao, D. Wan, X. Chen, X. Chao, and H. Xu, "Uniform breaking of liquid-jets by modulated laser heating," Phys. Fluids **33**, 044115 (2021).
[31]B. Jia, T. Wang, Q. Fu, and L. Yang, "Experimental study on the stability and breakup of a planar liquid sheet under a standing wave acoustic field," Phys. Rev. Fluids **7**, 124004 (2022).
[32]B. Jia, L. Xie, X. Deng, B. He, L. Yang, and Q. Fu, "Experimental study on the oscillatory Kelvin–Helmholtz instability of a planar liquid sheet in the presence of axial oscillating gas flow," J. Fluid Mech. **959**, A18 (2023).
[33]R. Qiao, K. Mu, X. Luo, and T. Si, "Instability and energy budget analysis of viscous coaxial jets under a radial thermal field," Phys. Fluids **32**, 122103 (2020).
[34]R. Qiao, K. Mu, and T. Si, "Analytical instability theory of a liquid jet under a thermal field," Acta Mech. Sin. **39**, 323086 (2023).
[35]S. Pal, H. Ryan, D. Hoover, and R. J. Santoro, "Pressure oscillation effects on jet breakup," in *Recent Advances in Spray Combustion: Spray Combustion Measurements and Model Simulation* (AIAA, 1996), pp. 233–259.
[36]J. Carpentier, F. Baillot, J. Blaisot, and C. Dumouchel, "Behavior of cylindrical liquid jets evolving in a transverse acoustic field," Phys. Fluids **21**, 023601 (2009).
[37]J. S. Hardi, H. C. G. Martinez, M. Oschwald, and B. B. Dally, "Lox jet atomization under transverse acoustic oscillations," J. Propul. Power **30**, 337–349 (2014).
[38]M. Gonzalez-Flesca, T. Schmitt, S. Ducruix, and S. Candel, "Large eddy simulations of a transcritical round jet submitted to transverse acoustic modulation," Phys. Fluids **28**, 055106 (2016).

[39]N. Rutard, L.-H. Dorey, C. Le Touze, and S. Ducruix, "Large-eddy simulation of an air-assisted liquid jet under a high-frequency transverse acoustic forcing," Int. J. Multiphase Flow **122**, 103144 (2020).
[40]T. Liu, X. Wang, and V. Yang, "Flow dynamics of shear-coaxial cryogenic nitrogen jets under supercritical conditions with and without acoustic excitations," Phys. Fluids **33**, 076111 (2021).
[41]J. O'Connor, V. Acharya, and T. Lieuwen, "Transverse combustion instabilities: Acoustic, fluid mechanic, and flame processes," Prog. Energy Combust. Sci. **49**, 1–39 (2015).
[42]R. Kelly, "The stability of an unsteady Kelvin–Helmholtz flow," J. Fluid Mech. **22**, 547–560 (1965).
[43]H. N. Yoshikawa and J. E. Wesfreid, "Oscillatory Kelvin–Helmholtz instability. Part 1. A viscous theory," J. Fluid Mech. **675**, 223–248 (2011).
[44]B. Jia, L. Xie, X. Cui, L. Yang, and Q. Fu, "Linear stability of confined coaxial jets in the presence of gas velocity oscillations with heat and mass transfer," Phys. Fluids **31**, 092101 (2019).
[45]X. Deng, H. Wang, X. Cui, L. Xie, and B. Jia, "Temporal instability of confined three-dimensional liquid jet with heat and mass transfer under longitudinal acoustic oscillations," Phys. Fluids **34**, 102107 (2022).
[46]S. Heister, M. Rutz, and J. Hilbing, "Effect of acoustic perturbations on liquid jet atomization," J. Propul. power **13**, 82–88 (1997).
[47]C. Yang, R. Qiao, K. Mu, Z. Zhu, R. X. Xu, and T. Si, "Manipulation of jet breakup length and droplet size in axisymmetric flow focusing upon actuation," Phys. Fluids **31**, 091702 (2019).
[48]X. Xu, Z. Zhu, K. Mu, F. Huang, and T. Si, "Parametric study on breakup of liquid jet in a gas-driven flow focusing process upon external excitation," Phys. Fluids **34**, 042001 (2022).
[49]C. Yang, Y. Yu, X. Wang, L. Shang, and Y. Zhao, "Programmable knot microfibers from piezoelectric microfluidics," Small **18**, 2104309 (2022).
[50]X. Yang and A. Turan, "Simulation of liquid jet atomization coupled with forced perturbation," Phys. Fluids **29**, 022103 (2017).
[51]C. R. Constante-Amores, L. Kahouadji, A. Batchvarov, S. Shin, J. Chergui, D. Juric, and O. K. Matar, "Direct numerical simulations of transient turbulent jets: Vortex-interface interactions," J. Fluid Mech. **922**, A6 (2021).
[52]D. Joseph, J. Wang, and T. Funada, *Potential Flows of Viscous and Viscoelastic Liquids* (Cambridge University Press, 2007).
[53]T. Funada and D. D. Joseph, "Viscous potential flow analysis of capillary instability," Int. J. Multiphase Flow **28**, 1459–1478 (2002).
[54]T. Funada, D. Joseph, and S. Yamashita, "Stability of a liquid jet into incompressible gases and liquids," Int. J. Multiphase Flow **30**, 1279–1310 (2004).
[55]H. Yang, "Asymmetric instability of a liquid jet," Phys. Fluids A **4**, 681–689 (1992).
[56]H. González, F. J. García, and A. Castellanos, "Stability analysis of conducting jets under ac radial electric fields for arbitrary viscosity," Phys. Fluids **15**, 395–407 (2003).
[57]A. Ruo, M. Chang, and F. Chen, "On the nonaxisymmetric instability of round liquid jets," Phys. Fluids **20**, 062105 (2008).